Decay of a Near-Inertial Wave

DAVE HEBERT

Graduate School of Oceanography, University of Rhode Island, Narragansett, Rhode Island

J. N. MOUM

College of Oceanic and Atmospheric Sciences, Oregon State University, Corvallis, Oregon

(Manuscript received 4 October 1993, in final form 14 March 1994)

ABSTRACT

The decay of a downward propagating near-inertial wave was observed over four days. During this short period, the energy of the near-inertial wave decreased by 70%. The shear layers produced by the wave were regions of enhanced turbulent dissipation rates. The authors estimate that 44% of the observed change in the near-inertial energy was lost to turbulence. Estimates of the wave energy lost at the survey site due to the wave propagating out of the region were smaller. Energy lost by horizontal advection of the wave out of the survey region was more difficult to estimate; the horizontal extent of the near-inertial energy was unknown. Advection could account for more than half of the observed energy lost. However, the authors did not detect the near-inertial wave during a 40 km × 40 km ADCP survey after completing the six-day station.

1. Introduction

Near-inertial oscillations are observed almost everywhere in the upper ocean, dominating the horizontal velocity of the internal wavefield. Because near-inertial waves also dominate the vertical shear (D'Asaro 1985; Kunze et al. 1990), they are believed to be especially important sources of mixing at the base of the surface mixed layer and deeper. In the upper ocean, downward propagating near-inertial waves are generally assumed to be the result of wind forcing. Much of the work to date [e.g., Pollard (1969), Gill (1984), D'Asaro (1985)] has examined the generation and decay of near-inertial oscillations in the surface mixed layer. The decay of these oscillations, usually expressed as a simple decay timescale O(2–10 days), represents the time for the waves to propagate out of the surface layer into the ocean interior. This decay timescale is dependent on the horizontal scale of the wind forcing and the β effect (D'Asaro 1989). Most of the initial near-inertial wave energy in the mixed layer leaves the forcing region by propagation. The lowest vertical modes have the largest group speeds; thus, they leave the forcing region first, leaving the higher mode near-inertial waves behind. Thus, near-inertial oscillations with relatively small vertical scales O(100 m) are usually observed below the surface mixed layer.

Corresponding author address: Dr. Dave Hebert, Graduate School of Oceanography, University of Rhode Island, Narragansett, RI 02882-1197.

The details of what happens to the near-inertial waves after they leave the mixed layer are relatively unknown. Modeling studies have looked at the vertical propagation of these waves (e.g., Rubenstein 1983), the horizontal propagation (e.g., Munk 1981) and the transfer of energy, via nonlinear dynamics, to other wavenumbers and frequencies (e.g., McComas and Müller 1981).

It is generally assumed that turbulent mixing observed in the main thermocline is due to internal waves (Gregg 1989). The internal waves either reach critical layers or a random superposition of internal waves produces local Richardson numbers below a critical value (e.g., 1/4) and mixing occurs (Munk 1981; Kunze et al. 1994). In some instances, advective instability of internal waves might be the source of turbulent mixing (Hebert et al. 1992; Moum et al. 1992). Most estimates of turbulent mixing have been made without direct measurements of internal waves. Only a few specialized profilers have the capability to obtain both the internal wave shear and turbulent dissipation rate (Gregg 1989; Toole and Schmitt 1987). However, shipboard acoustic Doppler current profilers (ADCPs) can resolve a significant fraction of the internal wave band (e.g., Chereskin et al. 1986), so it is possible to use the ADCP data in conjunction with turbulence measurements (Wijesekera et al. 1993).

In this paper, we examine the evolution and mixing produced by a near-inertial wave. Since near-inertial velocities are mainly horizontal and the horizontal wavelength is large compared to the separation of acoustic beams of the ADCP, a shipboard ADCP can

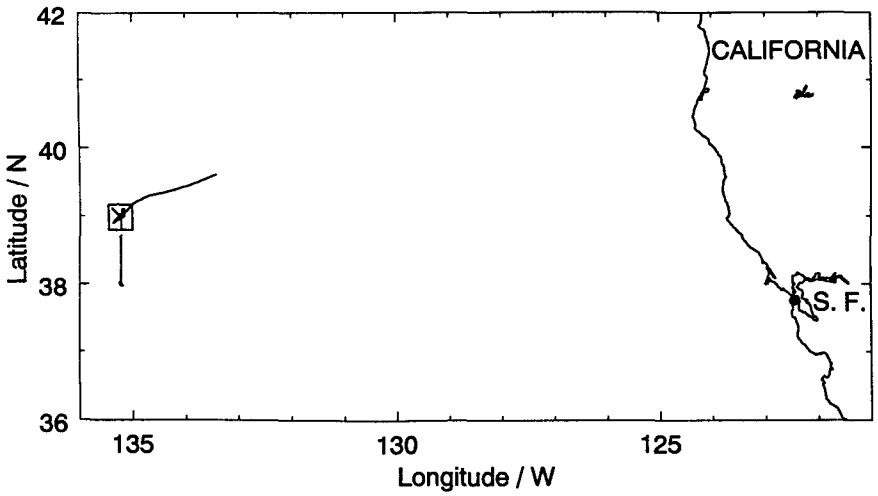

FIG. 1. Cruise track from 30 April 1991 (year day 120) to 9 May (YD 129). The time series station at 39°N was occupied from YD 122 to YD 128. The 40 km × 40 km box survey took approximately 12 h to complete, ending at YD 128 1425 UTC.

easily measure the velocity of near-inertial waves. Concurrent measurements of the turbulent kinetic energy dissipation rate, a surrogate of the turbulent mixing rate, were made also. The next section describes the instruments used and data collected. In section 3, the properties of the near-inertial wave are described. The dissipation rate and shear were highly correlated and both decreased after YD 126 (Fig. 3). [In this paper we define 1 January 1991 as year day 1 (e.g., YD 1). A fraction of a YD date represents the time of day (e.g., 1200 UTC on YD 1 is YD 1.5).] Was the enhanced turbulent dissipation observed in the shear layers responsible for the observed change in the near-inertial wave energy and the ultimate demise of the wave? The energetics and decay of the near-inertial wave are discussed in section 4.

2. Experimental details

In spring 1991, an experiment (FLUX STATS) to examine different estimates of turbulent heat flux in the upper ocean was conducted approximately 1000 km off the coast of California (Fig. 1). For approximately six days (YD 122–128), we occupied a single station (39°N, 135°15'W) where we made over 400 profiles to at least 650 m with the microstructure profiler CHAMELEON, an advanced version of the RSVP (Caldwell et al. 1985). After this station, we made a large-scale CTD/ADCP survey around a 40 km × 40 km box centered on our 6-day station before heading home (Fig. 1).

For the time-series station at 39°N, we obtained profiles of temperature, conductivity, and turbulent velocity shear and the vertical component of turbulent velocity approximately every 10 minutes. The larger-scale horizontal velocity field was determined using an RDI 150-kHz ADCP. A pulse length of 16 m and bin length of 8 m was used. (The half-power point of the vertical spatial response for this ADCP setting occurs at 40 m. Figure 3 of Lien et al. (1994) shows the vertical wavenumber response.) The ADCP data were averaged over 5 minutes before the data were stored. GPS-based navigation data was recorded every minute. These two datasets were combined into a single set of absolute velocities. Details of this procedure are described in Lien et al. (1994).

During this portion of the FLUX STATS experiment, three storms passed through this region (Fig. 2). The first occurred while we were 100 km south of the 39°N station and steaming toward the time-series station (Fig. 1). The second storm, which had higher peak winds but did not last as long, occurred after one day

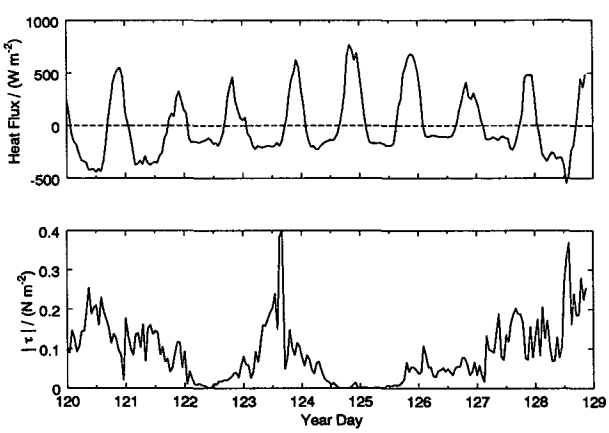

FIG. 2. Surface heat flux (upper panel) and wind stress magnitude (lower panel) determined from bulk formulas (Bahr and Paulson 1991, personal communication). Negative heat fluxes represent heat lost from the ocean.

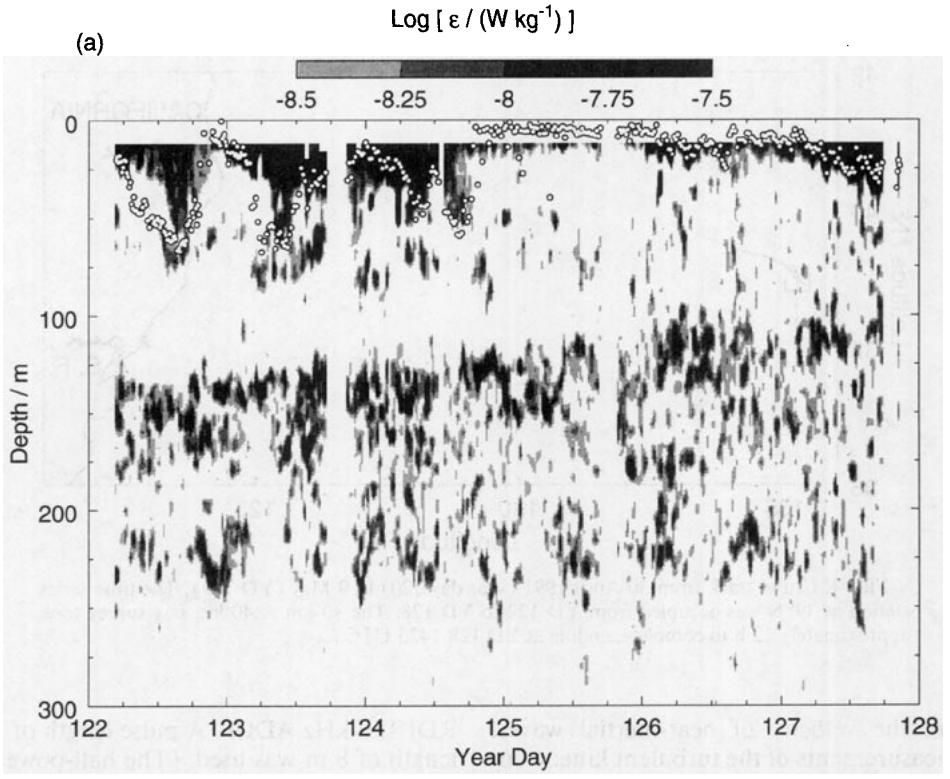

FIG. 3a. Turbulent kinetic energy dissipation rate ϵ for the 6-day time series at 39°N. For ease of viewing, dissipation rates above 3×10^{-8} W kg^{-1} are shaded black; values below 3×10^{-9} W kg^{-1} are white. The depth of the mixed layer (defined as the depth where the density exceeds the density at 2 m by 0.01 kg m^{-3}) is indicated by circles.

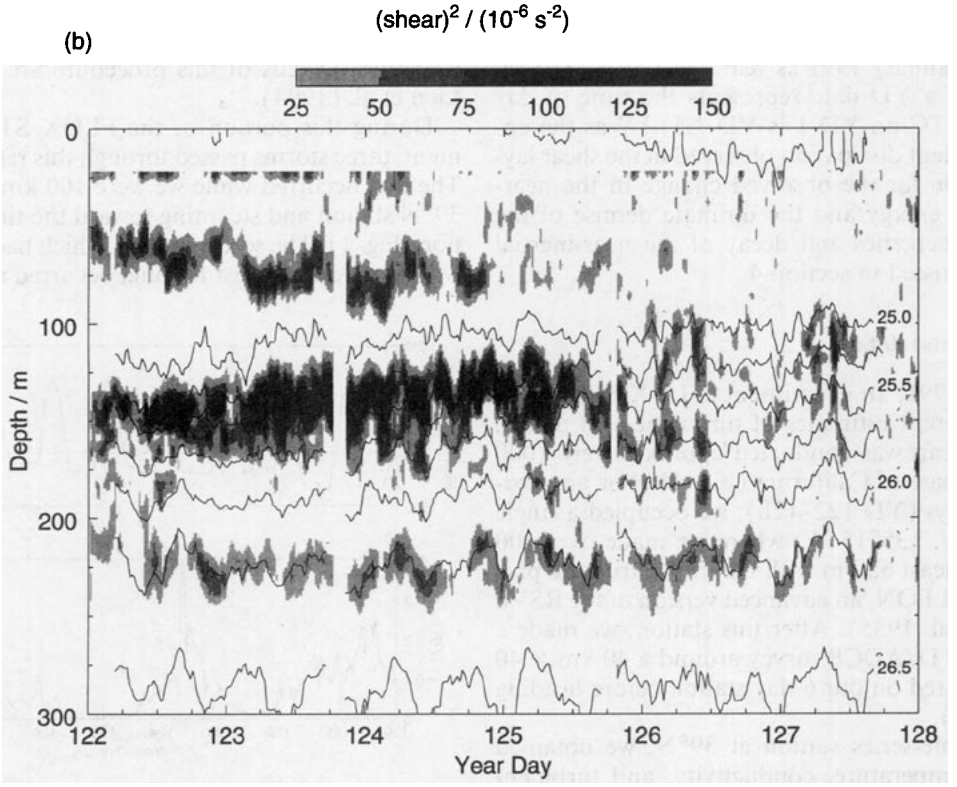

FIG. 3b. Square of the vertical shear of horizontal velocity [$S^2 = (\partial u/\partial z)^2 + (\partial v/\partial z)^2$] obtained by first differencing the ADCP data is shown by the shading. For ease of viewing, values greater than 1.5×10^{-4} s^{-2} are shaded black; values less than 2.5×10^{-5} s^{-2} are white. Contours of density (contour interval of 0.25 kg m^{-3}) are also shown.

on station. The third storm started near the end of the time series station and continued during our large-scale survey and transect home. The depth of the mixed layer (Fig. 3a) depended on both the strength of the wind and heating/cooling (Fig. 2). For example, the deepening of the mixed layer from YD 122.25 to 122.75 was most likely due to convection only during this time of nighttime cooling since the winds were weak. However, mixed layer deepening after YD 123 was a combination of wind and buoyancy forcing.

During the six-day time series at 39°N, we noticed two bands of high turbulent kinetic energy dissipation rate, ϵ, within the seasonal thermocline (Fig. 3a). These bands of high ϵ were correlated with regions of high vertical shear of horizontal velocity (Fig. 3b). The depth of both the shear and ϵ layers were advected vertically by the semidiurnal tide as evident from the density contours (Fig. 3b). Both the enhanced shear and ϵ decreased after YD 126. The source of these shear layers was a near-inertial wave described in the next section.

3. Near-inertial wave properties

In this section, we use the ADCP data to determine the properties of the near-inertial wave packet. Over YD 122–128, there was a low-frequency component to the velocity, especially in the upper ocean. A second-order polynomial fit (in time) to each velocity component at each depth was removed from the velocity data before further analysis. This low-frequency velocity consisted mainly of a mean current of 0.1 m s^{-1} to the northwest in the upper 150 m. In our determination of the intrinsic wave period, we assumed that horizontal advection of the wave and its horizontal and vertical propagation were small compared to its horizontal and vertical wavelengths; that is, any velocity variability at each depth was temporal, not spatial. Later, we will examine this assumption. In determining the period of the wave, we used only the data from YD 122 to 126, the time when the shear layers were clearly evident (Fig. 3b) (and, presumably, the observed velocity and shear were dominated by the near-inertial wave).

The ADCP velocities and shears showed an anticyclonic rotation (with time), indicative of an internal wave. Since the time series of the wave (whose amplitude is varying with time) is short compared to the wave period, two methods, complex demodulation and complex correlation, were used to estimate the period of the wave. These two methods also allow us to estimate the change in wave energy (via complex demodulation) or the decay time for the wave (via complex correlation). The complex correlation method also allows us to determine the wave period with higher accuracy than other methods such as Fourier analysis. These techniques, described in appendices A and B, were applied to both velocity and vertical shear data over a range of depths. A wave packet period of 18.6 h was chosen to represent the near-inertial wave period based on these different estimates of the wave period. The inertial period at this latitude is 19.07 h. Thus, the frequency of the near-inertial wave is $\omega = 1.025f$, where f is the inertial frequency.

The first method used to determine the near-inertial wave packet's period was complex demodulation. This technique is useful for generating a time series of the slowly varying amplitude of a wave with specified frequency as we will do later (section 4) in order to determine the wave energy and its temporal variability. Using complex demodulation, we determined the ellipse amplitude (major and minor axes) and orientation for a wave with known frequency that best describes the velocity (or shear) data. The amount of variance explained by this fitted wave (r^2) was determined also. To obtain the near-inertial wave period, we varied the frequency of the wave to maximize r^2 (see Fig. A1 for an example). Appendix A describes this procedure in more detail. Unfortunately, our velocity data was strongly contaminated by the semidiurnal tide (Fig. A1). Since the semidiurnal tide had a low vertical modal structure, it was not as evident in the shear data (Fig. A2). In appendix A, we describe the complex demodulation technique to determine the amplitude of two simultaneous waves (Poulain 1990) in order to determine the near-inertial wave energy with a semidiurnal wave present. In this way, the energy in the near-inertial wave band is clearly distinguished from that in the semidiurnal wave band.

Tidal velocities dominated the near-inertial signal for depths shallower than 75 m (Fig. 4). The combination of these two waves, the M_2 tide and a wave with a period of 18.6 h ($\omega = 1.025f$), explains more than 60% of the velocity variance in the upper 300 m (Fig. 4b). At 130 m, these two waves accounted for 80% of the velocity variance observed. The influence of the M_2 tide on the vertical shear was almost nonexistent (Fig. 5). At the depths of significant shear (Fig. 5a), more than 40% of the shear variance is associated with this single near-inertial wave (Fig. 5b).

For a single linear plane internal wave, the ratio of major to minor axes is ω/f. The ratio of the velocity ellipse axes (Fig. 4a) for the "M_2" wave predicts a frequency in agreement with that of the M_2 tide. The orientation of the ellipse (not shown) suggests that the M_2 tide was propagating meridionally. For the near-inertial wave, the ellipse was almost circular as expected. With the limited data available, the magnitude of the ellipse axes for the near-inertial wave observed (Figs. 4a and 5a) are not significantly different.

The second method used to estimate the period of the near-inertial wave packet was complex correlation (Gregg et al. 1986; summarized in appendix B). In examining the complex correlation of our data, the correlation was demodulated (i.e., rotated back clockwise) at a specified frequency. For a period of 18.6 h, the imaginary component of the demodulated complex

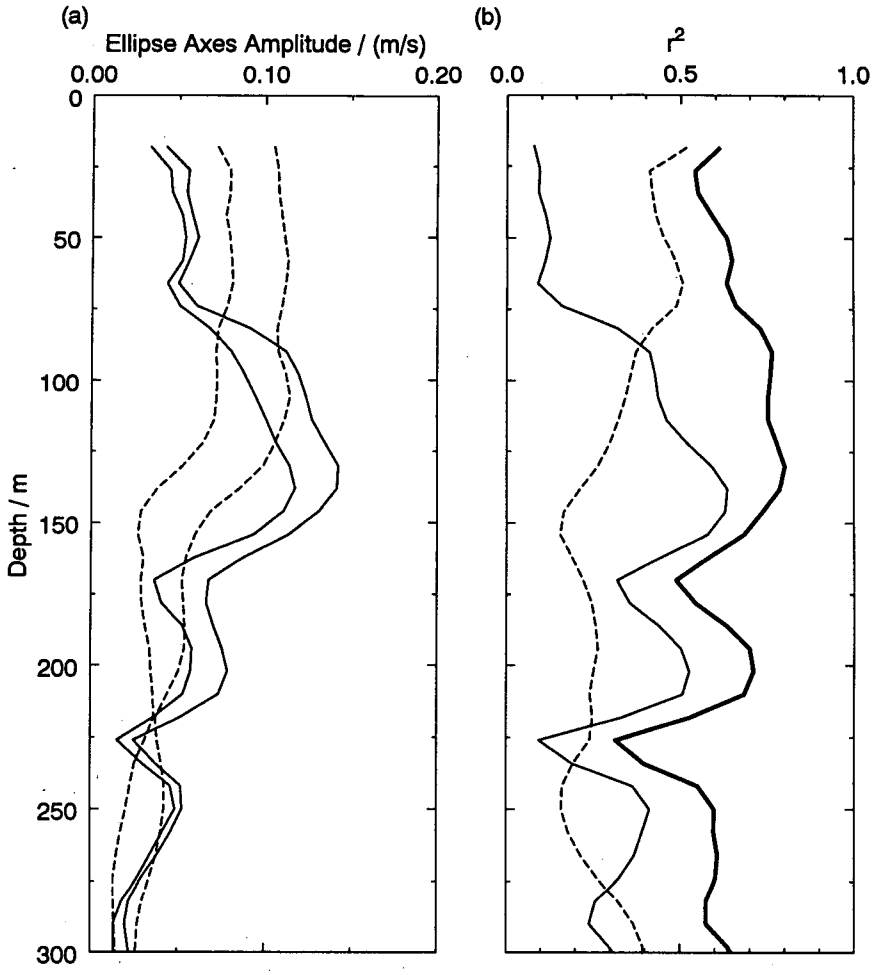

FIG. 4. (a) Amplitude of the velocity ellipse axes obtained from the complex demodulation of the near-inertial (period of 18.6 h was used) wave (solid lines) and the M_2 tidal component (dashed lines). (b) The velocity variance explained by near-inertial wave only (thin line), by the M_2 tidal component only (dashed line), and by both components together (thick line).

correlation for both the velocity (Fig. 6) and shear (Fig. 7) for the depth range 58–250 m showed no significant trend with increasing lag. This supports the near-inertial period determined from complex demodulation. If a slightly lower demodulation frequency was used, the imaginary component of the complex correlation would increase with lag (see appendix B). Likewise, a slightly higher demodulation frequency would have an imaginary component decreasing with lag. The demodulated complex correlation for the velocity data (Fig. 6) had an oscillation of both real and imaginary components—evidence of the M_2 tidal signal. The frequency of this oscillation is the difference in the M_2 tidal frequency and the demodulation frequency (appendix B).

Having estimated the period of the near-inertial wave packet, we can determine its vertical wavelength. As shown earlier, the velocity field was heavily contaminated by the M_2 tide, especially compared to the shear. Therefore, we will use the shear to determine the vertical wavelength. Since the stratification, N^2, varied vertically, the local vertical wavelength will change also. This influence can be removed by stretching the depth vertically using the WKB approximation [see Sanford (1991) for an excellent discussion of this technique]. For each 5-min shear vector, the WKB-stretched shear vector was rotated counterclockwise at the near-inertial wave frequency to a common time before averaging the shear vectors. This "back-rotation" removes the temporally oscillatory nature of the wave shear. The WKB-stretched (N_0 = 3 cph) shear[1] had a clockwise rotation with depth (Fig. 8). Over the depth range 46–350 WKB-stretched-m (58–250 m), the mean rotation of phase with depth gives a vertical wavelength of 146 WKB-stretched-m. Only using the phase when

[1] The magnitude of the shear was not WKB-scaled in Fig. 8.

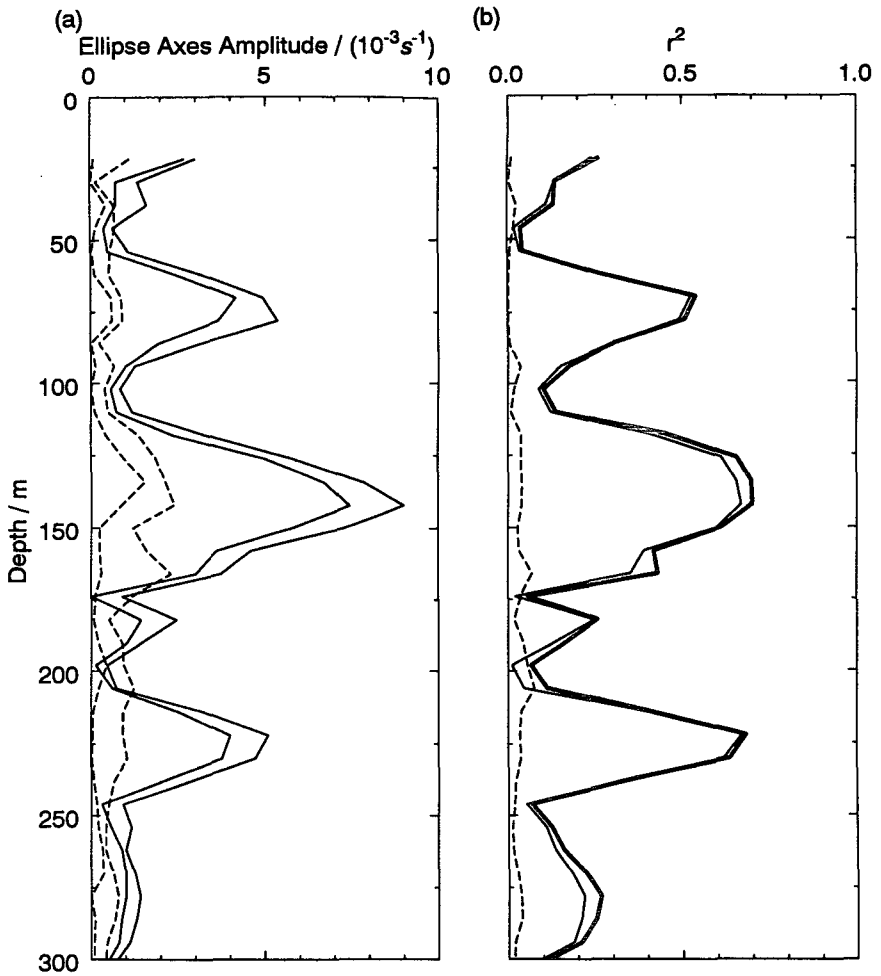

FIG. 5. (a) Amplitude of the shear ellipse axes obtained from the complex demodulation of the near-inertial (period of 18.6 h was used) wave (solid lines) and the M_2 tidal component (dashed lines). (b) The shear variance explained by near-inertial wave only (thin line), by the M_2 tidal component only (dashed line), and by both components together (thick line).

$|S| > 10^{-3}$ s^{-1}, the vertical wavelength would be 151 WKB-stretched-m. The vertical wavelength using the data between 54 and 238 WKB-stretched-m (~70 and 180 m) was 201 WKB-stretched-m. Similar vertical wavelengths are obtained if the shear data is back-rotated at the inertial period (19.07 h).

Using the dispersion relationship,

$$\frac{\omega}{f} = \left(1 + \frac{N^2\kappa_H^2}{f^2m^2}\right)^{1/2} \Big/ \left(1 + \frac{\kappa_H^2}{m^2}\right)^{1/2} \approx 1 + \frac{N^2\kappa_H^2}{2f^2m^2}, \quad (1)$$

the estimated frequency of the wave, $\omega/f = 1.025$, and the vertical WKB-stretched wavelength, $2\pi/m = 146$ WKB-stretched-m, the horizontal wavelength ($2\pi/\kappa_H$) of the near-inertial wave is 37 km (Table 1). For a vertical wavelength of 201 WKB-stretched-m, the horizontal wavelength would be 51 km. As expected, the larger the vertical wavelength, the larger the horizontal wavelength. Also, for a wave with a period closer to the inertial period, the horizontal wavelength is larger for the same vertical wavelength.

We reexamined our data to determine if a horizontal wavelength of 40–50 km and an intrinsic period of 18.6 h were consistent. In our determination of the wave period, we had assumed that the horizontal wavelength was large; with a mean advection velocity of 0.1 m s^{-1} over 4 days, the horizontal wavelength would have to be much larger than 35 km. Assuming that the near-inertial wave was passively advected through our survey region by the northwestward low-frequency current, the time series of shear observed at the ship consists of both temporal and spatial variability. At 150 m, the wave packet was advected approximately 20 km to the northwest (Fig. 9a). Back-rotating the shear vector with the wave frequency ($\omega = 1.025f$) to YD 122/0100 UTC, the shear vector was generally in a west by southwest direction at this time

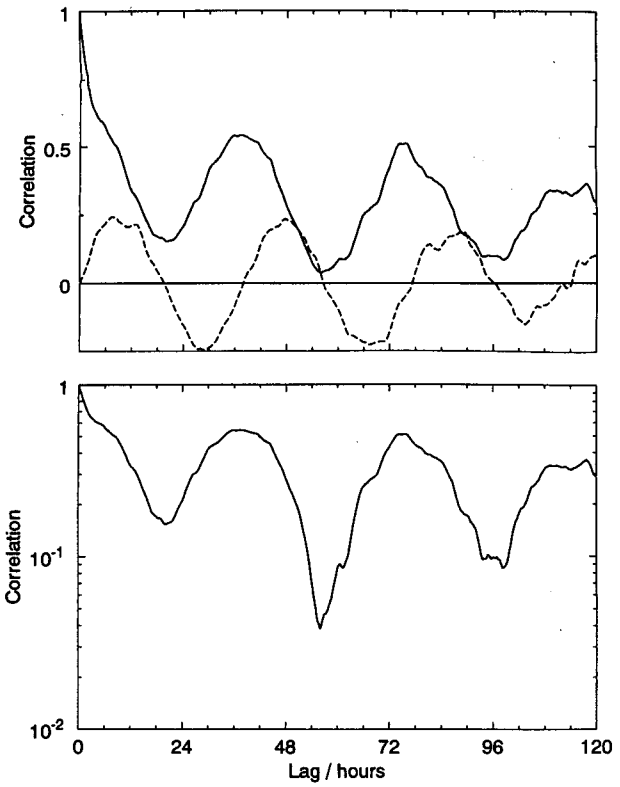

FIG. 6. Top panel: Real (solid line) and imaginary (dashed line) components of the demodulated complex correlation of velocity over the depth range 58–250 m. The demodulation frequency was $2\pi/18.6$ h. Bottom panel: Semilogarithmic plot of the real component of the demodulated complex correlation.

(Fig. 9b). If the shear was due only to a wave with period of 18.6 h, these rotated shear vectors would show the spatial structure of the wave; shear vectors located half a wavelength apart would point in opposite directions (a 180° phase shift). There was no evidence of a phase change with horizontal distance (Fig. 9b). The horizontal wavelength (in a northwest–southeast direction) must have been larger than 80 km. Using a higher frequency for the wave in order to produce an observable horizontal wavelength would not produce a proper alignment of the shear vectors with time. Adjacent shear vectors would point in different directions. If the shear vector is back-rotated at a lower frequency (e.g., the inertial frequency), there is a rotation of the shear vector in the northwest–southeast direction (Fig. 9c) although there is significant variability in the shear vector direction at a single location. This phase change of approximately 45° over 15 km gives a horizontal wavelength of approximately 120 km in the northwest–southeast direction. A pure inertial wave would have an infinite horizontal wavelength. A near-inertial wave with slightly higher frequency than an inertial wave would have a similar structure as shown in Fig. 9c. A near-inertial wave with the observed vertical wavelength 146 WKB-stretched-m and period of 19.02 h ($\omega = 1.002f$) would have a horizontal wavelength of 120 km (Table 2). Thus, the wavelength in the northwest–southeast direction must be approximately 120 km. We cannot estimate the horizontal wavelength of the wave in any other direction. With the data available, we cannot determine the exact intrinsic frequency and horizontal wavelength of the near-inertial wave.

In determining the near-inertial wave energy (next section), the results are the same for a wave of period 18.6 or 19.07 h (the inertial period). For the remainder of the paper, we will assume that the wave had an intrinsic period of 18.6 h. This choice only affects our estimate of the wave propagation speeds and energy fluxes by these processes. Propagation speeds are larger for a wave of period 18.6 h than a wave of frequency closer to the inertial frequency (Tables 1 and 2). Hence, our energy flux estimates due to wave propagation in section 4 represent upper bounds.

In our discussion of the near-inertial wave energetics, it is necessary to determine the wave propagation speeds in order to estimate the flux of wave energy out of our survey region. Given the estimated properties of the near-inertial wave (Table 1) and assuming linear

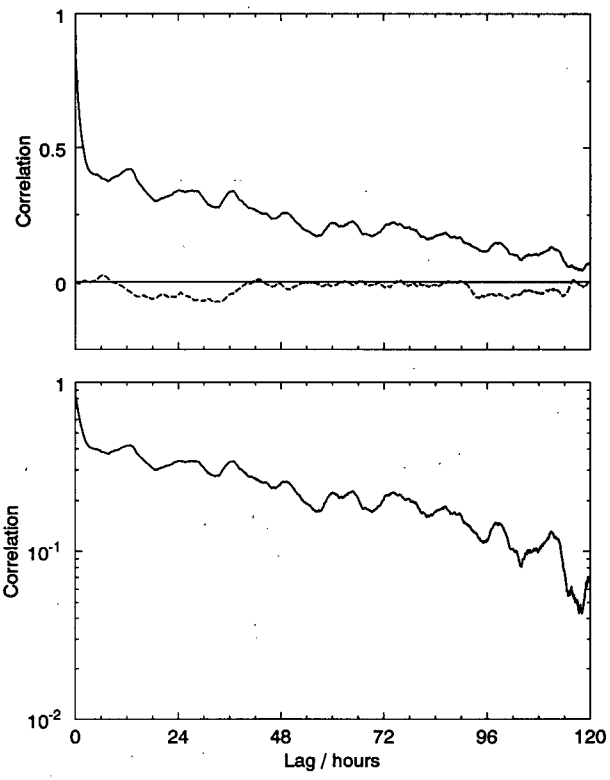

FIG. 7. Top panel: Real (solid line) and imaginary (dashed line) components of the demodulated complex correlation of shear over the depth range 58–250 m. The demodulation frequency was $2\pi/18.6$ h. Bottom panel: Semilogarithmic plot of the real component of the demodulated complex correlation.

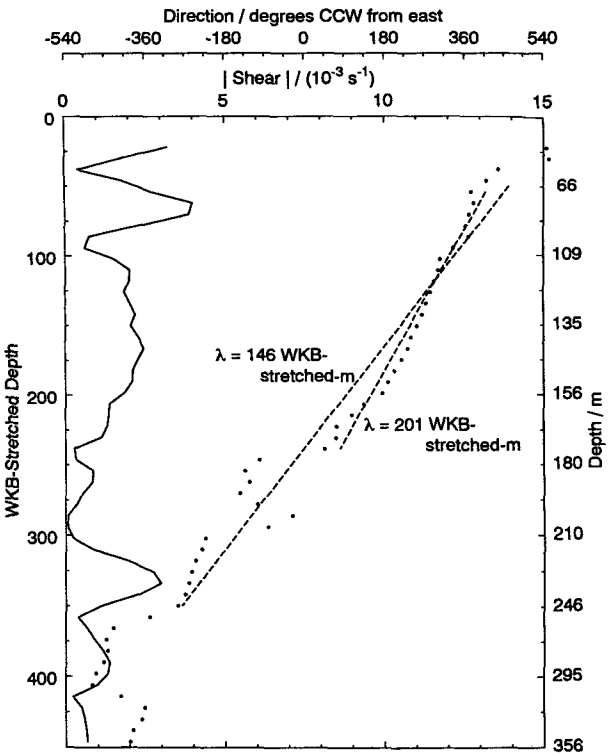

FIG. 8. Average (YD 122–126) magnitude (solid line) and phase (dotted line) of the shear as a function of the WKB-stretched depth. The shear vector was back-rotated (counterclockwise) by the near-inertial period (18.6 h) to a common time, and the depth was WKB-stretched before averaging. Approximate true depths are shown on the right-hand side. Estimates of the vertical wavelength were obtained from least squares regression to the phase (dashed lines). The dashed lines also show the depth range over which the least squares regression was determined.

internal wave dynamics, the horizontal and vertical phase and group speeds can be determined. The vertical propagation of the wave energy was very slow, only 10 m day^{-1}. Over the 4-day period, we did not detect significant vertical propagation of the shear layers (Fig. 3b). For near-inertial waves with the same vertical wavelength, the vertical and horizontal group speeds decrease as the wave period approaches the inertial period. For example, a wave of period 19.02 h ($\omega = 1.002f$) and vertical wavelength 146 WKB-stretched-m has vertical group speed of 1.0×10^{-5} m s^{-1} (1 m day^{-1}) and horizontal group speed of 8.5×10^{-3} m s^{-1} (750 m day^{-1}).

4. Decay of the wave

Having determined the general properties of the near-inertial wave, we examine mechanisms responsible for the observed change in the near-inertial wave energy. The energy (density) equation for the wave,

$$\frac{\partial E}{\partial t} + \nabla\cdot(\mathbf{c}_g E) + \nabla\cdot(\mathbf{u}E) - \epsilon - B - S = 0, \quad (2)$$

is a balance between the local change in energy density at a fixed location, propagation, and advection of the wave packet energy out of our observation region, dissipation of the energy by turbulence, conversion of wave energy to mean potential energy, and other sinks such as the transfer of energy to waves with other frequencies and wavelengths. In a rotating fluid, the mean flow can only absorb the near-inertial wave energy through turbulent mixing (Kunze et al. 1994).

For near-inertial waves, the ratio of kinetic energy due to the vertical velocity (VKE) to that due to the horizontal velocity (HKE; commonly referred to as the horizontal kinetic energy) is

$$\frac{\text{VKE}}{\text{HKE}} = \frac{(\omega^2 - f^2)}{(\omega^2 + f^2)} \frac{\omega^2}{(N^2 - \omega^2)}, \quad (3)$$

which is approximately 1/125 000 for our near-inertial wave. The ratio of available potential energy (PE) to horizontal kinetic energy can be expressed as

$$\frac{\text{PE}}{\text{HKE}} = \frac{(\omega^2 - f^2)}{(\omega^2 + f^2)} \frac{N^2}{(N^2 - \omega^2)}, \quad (4)$$

which is 1/40 for our near-inertial wave. Therefore, we can assume that the kinetic energy based only on the horizontal velocity represents the total wave energy. Turbulence studies (Oakey 1982; Moum et al. 1989) show that the buoyancy production (B) is approximately 20% of ϵ. Since we are only examining the relative importance of the terms in (1) and not trying to close the energy budget, we will ignore B in (2). Thus, the energy equation for a near-inertial wave is

TABLE 1. Properties of the observed near-inertial wave. The period and vertical wavelength were estimated from the ADCP data. The horizontal wavelength and phase and group speeds were obtained from the linear internal wave dispersion relationship. The inertial period at this latitude is 19.07 h ($f = 9.15 \times 10^{-5}$ s^{-1}).

Period (h)	T		18.6	
Nondimensional frequency	ω/f		1.025	
Vertical wavelength (WKB-stretched-m)	λ_z	146		201
Horizontal wavelength (km)	λ_H	36.9		50.8
Vertical phase speed (m s^{-1})	c_{pz}	2.18×10^{-3}		3.00×10^{-3}
Horizontal phase speed (m s^{-1})	c_{pH}	5.51×10^{-1}		7.59×10^{-1}
Vertical group speed (m s^{-1})	c_{gz}	-1.06×10^{-4}		-1.46×10^{-4}
Horizontal group speed (m s^{-1})	c_{gH}	2.68×10^{-2}		3.69×10^{-2}

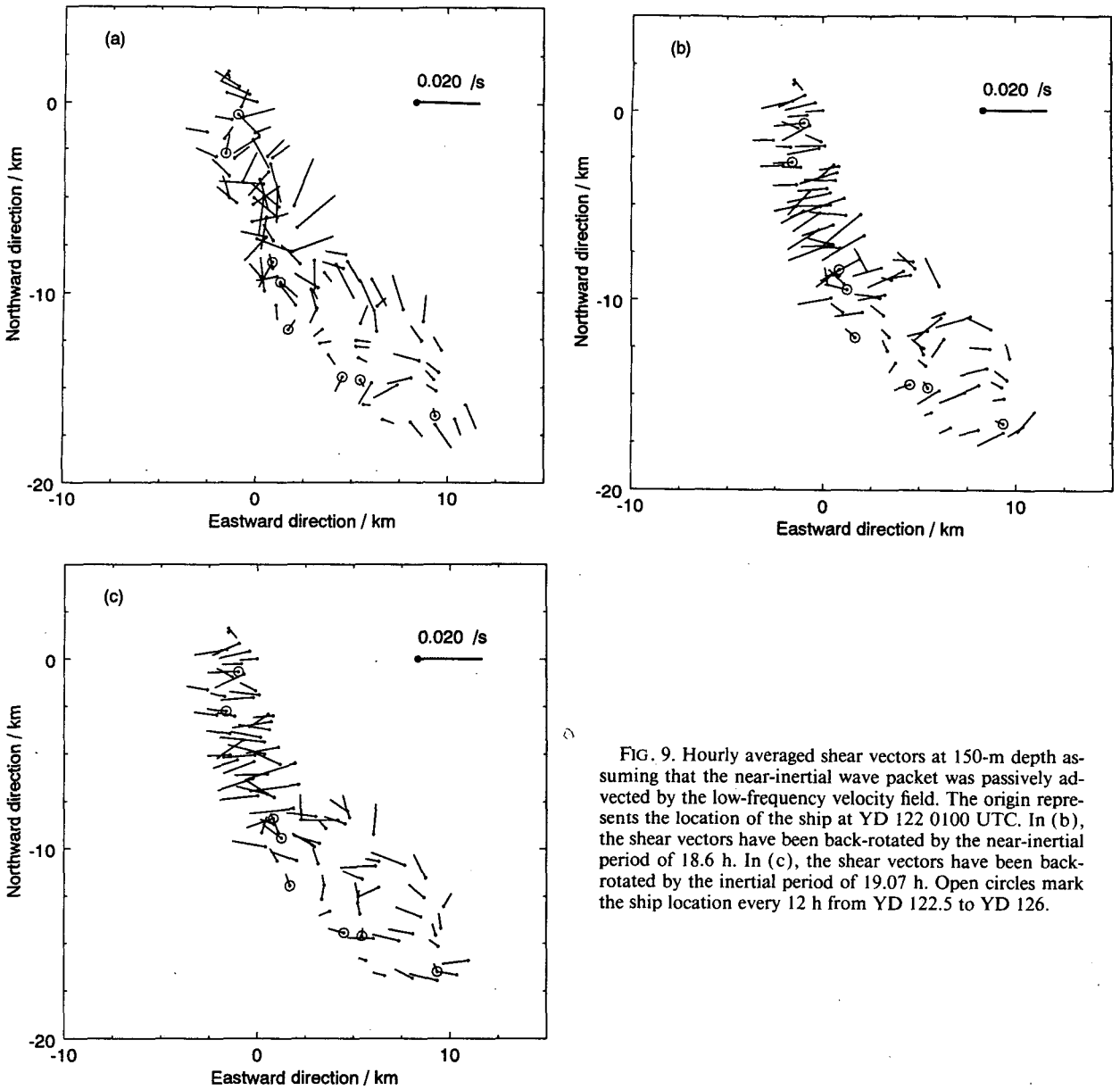

FIG. 9. Hourly averaged shear vectors at 150-m depth assuming that the near-inertial wave packet was passively advected by the low-frequency velocity field. The origin represents the location of the ship at YD 122 0100 UTC. In (b), the shear vectors have been back-rotated by the near-inertial period of 18.6 h. In (c), the shear vectors have been back-rotated by the inertial period of 19.07 h. Open circles mark the ship location every 12 h from YD 122.5 to YD 126.

$$\frac{\partial(\mathrm{HKE})}{\partial t} + \mathbf{u}_H \nabla_H(\mathrm{HKE}) + \mathbf{c}_{gH} \nabla_H(\mathrm{HKE}) + c_{gz} \frac{\partial}{\partial z}(\mathrm{HKE}) - S - \epsilon = 0. \quad (5)$$

Integrating (5) over a specified time interval (e.g., the period of reliable estimates of HKE as described below), the equation describing the change in wave energy is

$$\Delta\mathrm{HKE} + \int \mathbf{u}_H \nabla_H(\mathrm{HKE})\,dt + \int \mathbf{c}_{gH} \nabla_H(\mathrm{HKE})\,dt + \int c_{gz} \frac{\partial}{\partial z}(\mathrm{HKE})\,dt - \int S\,dt - \int \epsilon\,dt = 0. \quad (6)$$

With our data from the ADCP and CHAMELEON, we can estimate the first and last terms on the left-hand side of (6). We will also estimate the three terms representing the horizontal and vertical energy flux given our general knowledge of the wave's properties. The other sinks of wave energy, such as wave–wave interaction, are harder, if not impossible, to estimate.

a. ΔHKE

To determine the change in HKE, we use the complex demodulation technique for two waves described in appendix A. A time interval must be chosen over which to demodulate the velocity data, long enough to

TABLE 2. Phase and group speeds of a near-inertial wave with period 19.02 h, horizontal wavelength 120 km and vertical wavelength 146 WKB-stretched-m.

Period (h)	T	19.02
Nondimensional frequency	ω/f	1.002
Vertical wavelength (WKB-stretched-m)	λ_z	146
Horizontal wavelength (km)	λ_H	120
Vertical phase speed (m s^{-1})	c_{pz}	2.13×10^{-3}
Horizontal phase speed (m s^{-1})	c_{pH}	1.75
Vertical group speed (m s^{-1})	c_{gz}	-1.03×10^{-5}
Horizontal group speed (m s^{-1})	c_{gH}	8.46×10^{-3}

allow a reliable estimate of the amplitude of the waves (e.g., several wave periods) but short compared to the length of the 6-day time series and the rate at which the wave amplitude changes. To reduce the error in the amplitude estimate, especially for short time intervals, it is best if the time interval is an integer multiple of half the wave period. We chose a time interval of 55.8 h over which to demodulate the ADCP data. This interval is three periods of the near-inertial wave and approximately 4 1/2 periods of the M_2 tide. We determined the average HKE of both the near-inertial wave and M_2 tide at each ADCP depth bin and for every 6 hours from YD 122.25 to YD 127.75[2] (Fig. 10). The M_2 tidal energy was strongest near the surface and reached a maximum around YD 124.3. The near-inertial wave energy was mainly located between 75 and 200 m. However, there appears to have been significant near-inertial wave energy in the mixed layer before YD 123. The storm that occurred around YD 123.5 (Fig. 2) did not produce any significant inertial wave energy in the mixed layer (Fig. 10a). For this storm, most of the wind energy appears to have gone into deepening the surface mixed layer (Fig. 3a). Rotation of the wind stress vector for this storm was almost nonexistent or slightly counterclockwise while the wind stress for the earlier storm (YD 120–122) had a clockwise rotation with time. D'Asaro (1985) showed that a wind stress with clockwise rotation with time will pump more energy into the inertial wave field. Below the mixed layer, the overall near-inertial wave energy decreased after YD 123.5.

Since the vertical propagation of the wave was unobservably small, we have not WKB-scaled HKE. This lack of scaling does not affect our results on the overall energetics of the near-inertial wave, it only changes the vertical distribution of the energy density. The WKB-scaled HKE (Sanford 1991) has a vertical distribution similar to that in Fig. 10a except that the maximum energy density is located at 98 instead of 138 m, the depth of the maximum in the buoyancy frequency.

With these near-inertial HKE estimates, we can examine the change in the wave's vertically averaged HKE. We chose the depth range 58 to 250 m to ensure that the large shear and dissipation regions were and the mixed layer was not included (Fig. 3). Other vertical averaging limits were examined and produced similar results.

The depth-averaged HKE of the wave decreased from 5.0 to 1.6 ($\times 10^{-3}$ J kg^{-1}) over 4 days (Fig. 11a). The decay of the wave energy appears to have been exponential with an e-folding time of 3 days. The complex correlation of the shear over this depth range showed a similar decay time (Fig. 7).

The observed change in the depth-averaged near-inertial energy at a fixed point can be compared to the turbulent dissipation rate and some of the other terms in (6).

b. $\int \epsilon dt$

The depth-averaged turbulent kinetic energy dissipation (smoothed with a 55.8-h boxcar filter) shows an enhanced dissipation rate at the time when the change in the wave's HKE was the greatest (Fig. 11b). This enhancement of dissipation between YD 123 and 125.5 is more evident if a shorter smoothing filter is used. The time-integrated turbulent dissipation rate ($\int \epsilon\, dt$) is approximately 44% of the observed change in HKE over the four days (Fig. 11c and Table 3). In this comparison, we had assumed all the observed ϵ to originate directly from energy lost by the near-inertial wave. However, there is always some level of the turbulent dissipation in the thermocline due to the random superposition of internal waves of different frequencies and wavenumbers. If we assume that there was a background ϵ, unrelated to the near-inertial wave, of 3×10^{-9} W kg^{-1} based on the 6-h average dissipation over the same depth range at the start and end of our time series when the average dissipation rate was at a minimum,[3] the turbulent dissipation above this background value would account for 14% of the observed change in HKE.

c. $\int c_{gz} \partial(\mathrm{HKE})/\partial z dt$

To estimate the change in HKE due to the vertical propagation, it is necessary to estimate the vertical gradient of HKE and use the group speed obtained earlier (Table 1). Estimating the average energy lost this way is not straightforward. However, we can estimate the amount of energy that would propagate

[2] For times before YD 123.2 and after YD 126.8, the time interval of data for the demodulation was less than 55.8 h and not symmetrically located about the central time. These regions in Fig. 10 will have a large error associated with them and have been presented only to emphasize the general trend in the figure.

[3] This dissipation rate is likely an overestimate of the background ϵ since the near-inertial wave shear is probably producing mixing even if it is lower than the peak dissipation rates observed between YD 123 and YD 127.

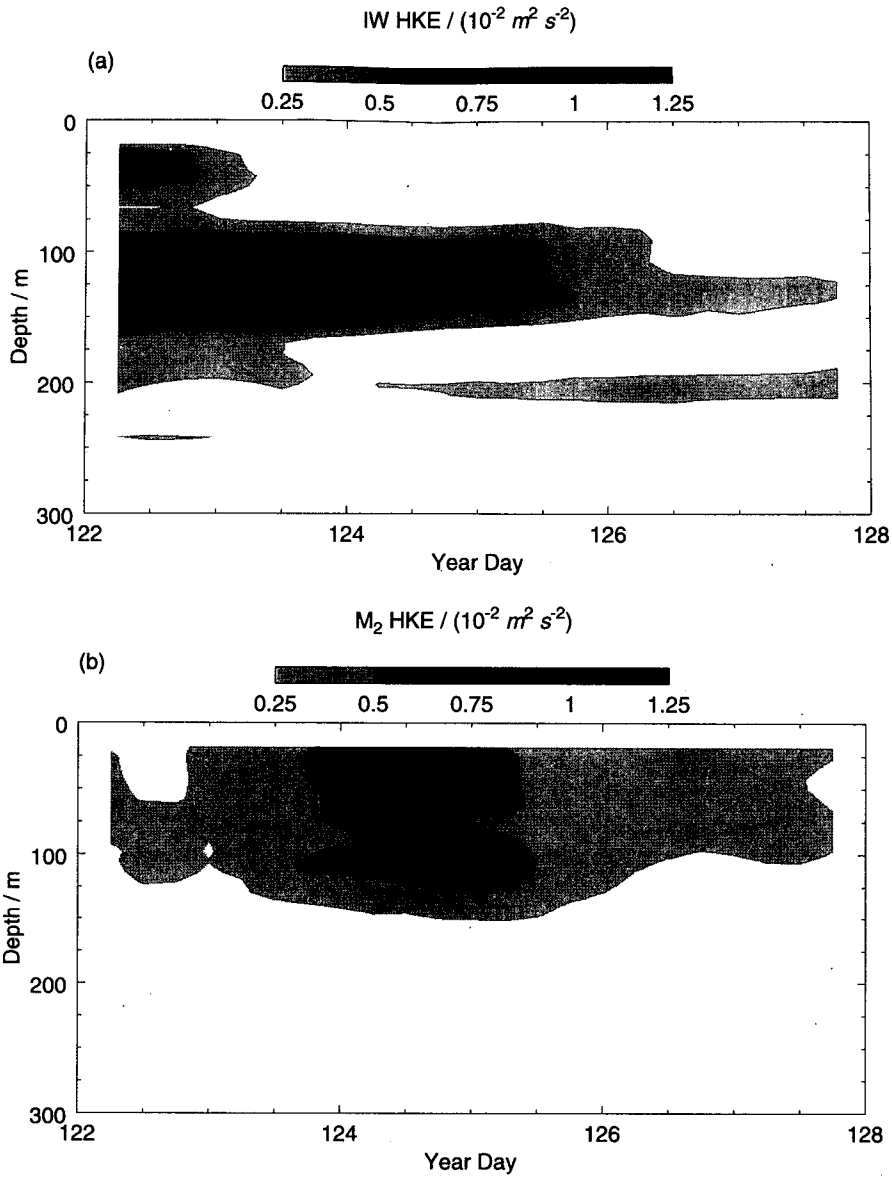

FIG. 10. The kinetic energy due to the horizontal velocity (HKE) for the (a) near-inertial wave and (b) M_2 tide obtained from complex demodulating the ADCP data over a 55.8-h period every 6 h.

vertically out of the averaging region (58–250 m) over four days. If the vertical distribution of HKE is represented by a sinusoid [centered in the averaging region (58–250 m) on YD 123], vertical propagation of this energy distribution ($c_{gz} = 1.5 \times 10^{-4}$ m s^{-1}) would account for a change of 8×10^{-4} J kg^{-1} in the depth-averaged HKE over four days. This energy loss due to vertical propagation of the wave (VP) is only 24% of the observed change in HKE (Fig. 11c). The actual energy lost by VP is less. With this vertical group speed, the near-inertial energy would be 52 m deeper after four days. Our velocity data showed no evidence of vertical propagation (Figs. 3 and 10a).

d. $\int c_{gH} \nabla_H (\mathrm{HKE}) dt$

The horizontal energy flux is more difficult to estimate. We do not know the horizontal gradient of HKE or even the horizontal extent of the near-inertial wave at the start of our measurements. For our energy loss estimate, we assume that $\nabla_H(\mathrm{HKE}) = \Delta\mathrm{HKE}/35$ km, the observed change in HKE occurred over the distance it was advected in 4 days. The energy loss due to hor-

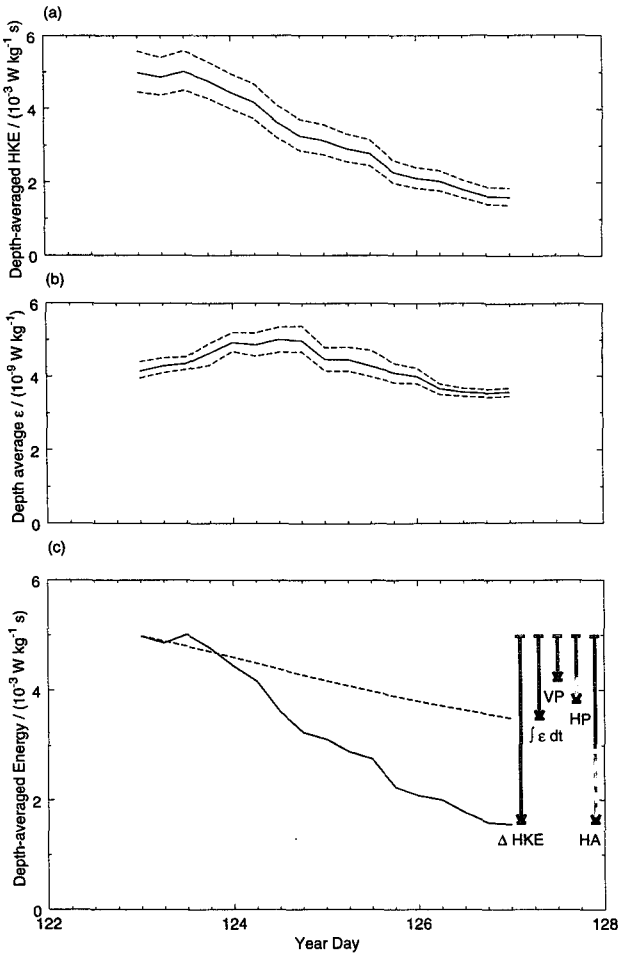

FIG. 11. (a) The depth-averaged (58–250 m) near-inertial wave horizontal kinetic energy. Dashed lines represent the 95% confidence limits obtained by the bootstrap method (Efron and Gong 1983). (b) The depth-averaged (58–250 m) turbulent kinetic energy dissipation rate. Dashed lines represent the 95% confidence limits. (c) The depth-averaged HKE from (a) (solid line) and the time-integrated turbulent kinetic energy dissipation rate (dashed line). The left-hand side of the figure shows the total change in energy obtained from the observed change in HKE (ΔHKE) and the turbulent dissipation ($\int \epsilon\, dt$). Estimates of energy lost due vertical (VP) and horizontal (HP) propagation of the wave and horizontal advection (HA) are also shown. For VP and HP, the total length of the arrow is the estimate based on a wave packet 70 km wide; the solid portion of the arrow is the estimate based on a wave packet 120 km wide. See the text for more details.

izontal propagation (HP) would be 35% of the observed ΔHKE (Fig. 11c and Table 3). The choice of the horizontal length scale above was arbitrary. Near-inertial wave packets are frequently observed to be one wavelength wide (E. Kunze 1994, personal communication). If we assume that the horizontal scale of the wave was 120 km, an estimate of the horizontal wavelength (see section 3), then HP accounts for 21% of ΔHKE (Fig. 11c and Table 3). Another way to examine the energy lost by HP is to assume that all the observed change in HKE was due to horizontal propagation. If so, the horizontal scale of the wave would have been smaller than 25 km. This is unlikely for a near-inertial wave.

e. $\int \boldsymbol{u}_H \nabla_H(\mathrm{HKE})\,dt$

The horizontal advection of wave energy can be determined in a similar manner to the horizontal propagation above. As with that calculation, we have to assume a value for $\nabla_H(\mathrm{HKE})$. As expected, using the value above, ΔHKE/35 km, the change in HKE due to horizontal advection (HA) accounts for all of ΔHKE (Fig. 11c and Table 3). Also, the horizontal scale of the wave must have been less than 70 km, which is possible but unlikely. Using a 120-km horizontal scale for the wave packet, HA would account for 59% of ΔHKE (Fig. 11c and Table 3).

With our data, we cannot eliminate the possibility that all of the change in near-inertial energy was due to horizontal advection of the energy. However, we are confident that approximately 44% of ΔHKE was removed by turbulence. The remainder of ΔHKE could be due to horizontal advection of the near-inertial energy. On YD 128, we completed a large-scale (40 km × 40 km box) ADCP survey around the 39°N station. There was no sign of any shear layers in the upper thermocline. This would lead us to believe that the near-inertial wave had not propagated or been advected out of the survey region. Any energy flux of the near-inertial energy to the mean flow must be done by irreversible processes (Kunze et al. 1994) and is included in our turbulence dissipation rate estimate. We cannot eliminate the possibility that some of ΔHKE is due to wave–wave interactions or that the observed near-inertial energy was not due to a single near-inertial wave (see section 5).

5. Discussion

It is unfortunate that our observations did not include the near-inertial wave's full evolution. Although we know that it was propagating downward, we do not know when it was generated. Assuming that the observed wave propagated from the base of the surface mixed layer at 50-m depth to 125 m (the observed mid-depth of the wave) with a speed of 1.5×10^{-4} m s^{-1} (Table 1), this near-inertial wave would have been generated approximately 6 days before our arrival. For large-scale wind forcing, D'Asaro (1989) found that the β effect finally determines the meridional extent of surface generated near-inertial waves [e.g., $L_y = (\beta \Delta t)^{-1}$, where Δt is the time since the near-inertial wave was generated]. Thus, at the time of our observation, the meridional scale of the near-inertial wave must have been smaller than 100 km.

Since the storm that produced the observed near-inertial wave occurred well before we arrived, we cannot determine the inertial wave energy generated in

TABLE 3. The observed depth-averaged (58–250 m) change in horizontal kinetic energy of the near-inertial wave and the amount of energy dissipated by turbulence for the same region and time; 95% confidence limits are in parentheses. Estimates of energy lost by the propagation and advection of the wave out of our survey region are given. For VP, an upper limit of the energy lost is presented. For estimates of HP and HA, a range of energy lost is given (the lower and upper values correspond to wave packets 120 km and 70 km wide).

Change in near-inertial wave horizontal kinetic energy	ΔHKE	3.4×10^{-3} J kg^{-1} ($\pm 0.6 \times 10^{-3}$ J kg^{-1})
Energy dissipated by turbulence	$\int \epsilon dt$	1.49×10^{-3} J kg^{-1} ($\pm 0.05 \times 10^{-3}$ J kg^{-1})
Vertical propagation	VP = $\int c_{gz} \frac{\partial}{\partial z}$ (HKE)dt	$< 0.8 \times 10^{-3}$ J kg^{-1}
Horizontal propagation	HP = $\int c_{gH} \nabla_H$ (HKE)dt	$0.7 \rightarrow 1.2 \times 10^{-3}$ J kg^{-1}
Horizontal advection	HA = $\int u_H \nabla_H$ (HKE)dt	$2.0 \rightarrow 3.4 \times 10^{-3}$ J kg^{-1}

the mixed layer by the storm. However, D'Asaro (1985) found that April storms further north at OWS P (50°N, 145°W) generated on average a near-inertial energy of approximately 10^{-2} m^2 s^{-2} in the mixed layer. We speculate that near-inertial energy observed at the beginning of our measurements was approximately half the surface-forced internal wave energy and that approximately one-quarter of this energy was dissipated rapidly in the upper thermocline. Our ADCP time series is too short to determine if all the near-inertial energy disappeared by YD 128, that is, before the wave could have propagated deeper into the ocean interior.

The turbulent decay time for internal waves is $\tau = \langle E \rangle / \langle \epsilon \rangle$, where $\langle E \rangle$ is the average internal wave energy and $\langle \epsilon \rangle$ is the average dissipation rate. Using our average values for $\langle E \rangle$ and $\langle \epsilon \rangle$ (3.2×10^{-3} m^2 s^{-2} and 4.3×10^{-9} m^2 s^{-3}, respectively), our decay time is 9 days. Gregg et al. (1986) found a decay time of 4–8 days for their slightly more energetic near-inertial wave. Using Gregg's (1989) parameterization for ϵ (see discussion below), Marmorino and Trump (1991) estimate a decay time of 37 days for an upward propagating near-inertial wave. This is a typical value for the (total) internal wave decay observed in the seasonal thermocline (Gregg and Sanford 1988) or obtained from wave–wave interaction models (McComas and Müller 1981).

Although we estimate the turbulent dissipation of near-inertial energy and its energy fluxes either by propagation or advection, we cannot rule out the possibility that the near-inertial wave we observed was really two (or more) near-inertial waves beating against one another. At the start of the measurements, these two waves could have been in-phase and, by the end of our 6-day station, they could have been 180° out of phase. Thus, it would appear as though the wave had been dissipated. Imagine that the observed near-inertial shear (Fig. 8) was due to two near-inertial waves with the same horizontal wavelength of 80 km beating together. Two waves of vertical wavelengths 130 and 440 WKB-stretched-m would beat together to produce an apparent single wave with a wavelength of 200 WKB-stretched-m and an amplitude envelope of 185 WKB-stretched-m. From the dispersion relationship, the period of the two waves would be 18.988 ($\omega = 1.004f$) and 18.180 h ($\omega = 1.049f$), respectively. It would take these two waves 9 days to become 180° out of phase. (Using the same vertical wavelength and a 120 km horizontal wavelength, it would take 20 days for the two waves to become out of phase.) Therefore, it may be possible that the frequencies of the near-inertial waves producing the observed shear were such that they

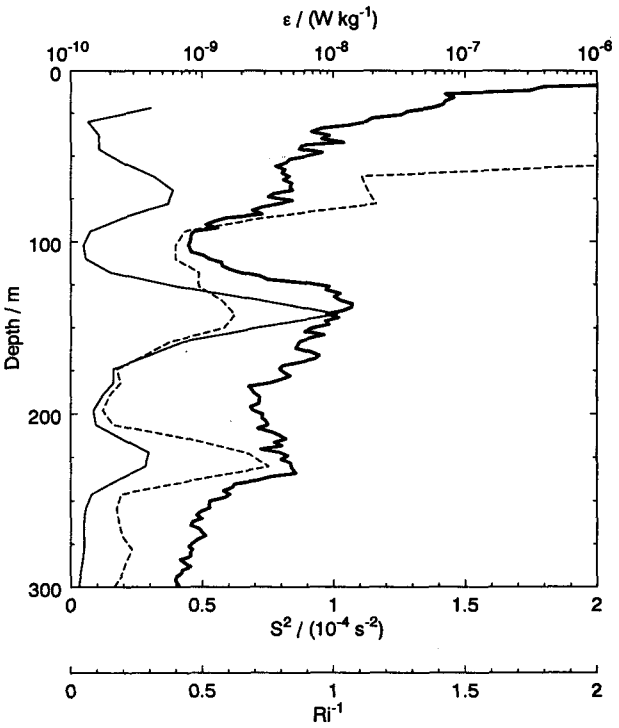

FIG. 12. YD 122–126 average profile of ϵ (thick solid line), S^2 (thin solid line), and Ri^{-1} (dashed line); S^2 was determined by first-differencing the velocity data, which are in 8-m bins. The stratification used in Ri^{-1} was the mean gradient in potential density over 8 m vertically.

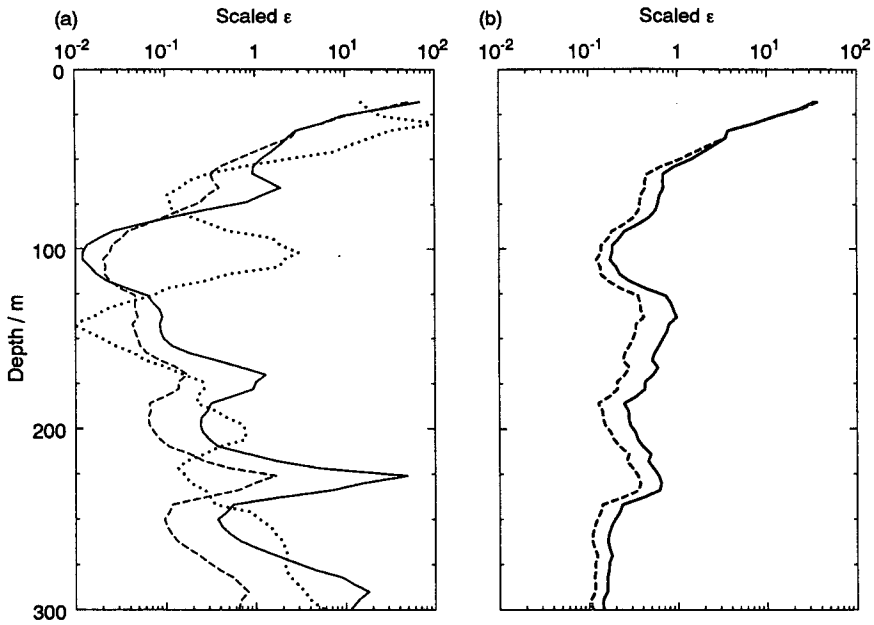

FIG. 13. The average dissipation rate ϵ (shown in Fig. 12) scaled by the different internal wave scalings described in the text. An arbitrary constant was chosen to center the profiles around a value of approximately 1. (a) The scalings based on the near-inertial wave energy (ϵ_{IW}: solid line, ϵ_{GA}: dashed line, and ϵ_{G89}: dotted line). (b) The scaling based on just stratification (ϵ_{GH1}: solid line, ϵ_{GH2}: dashed line).

became out of phase after YD 126. Only a much longer time series would disprove this scenario; the near-inertial energy would increase as the waves became in phase again.

Over the observation period, the location of high-ϵ layers tracked the high-shear layers. This result differs from that found by Gregg et al. (1986). They found that their turbulent patch started in the high-shear region below the near-inertial wave velocity maximum and rose into the region of the maximum, remaining there for most of the duration of the turbulent patch (3 days). This result led Gregg et al. (1986) to conclude that critical-layer absorption might be responsible for the mixing. Our result suggests that near-inertial shear induces instability responsible for the mixing. For shorter time series (15 h), Marmorino et al. (1987) found that turbulent mixing based on high-frequency temperature fluctuations coincided with high shear, leading to the same conclusion.

Recently, there have been many attempts to relate turbulent dissipation (mixing) to properties of the internal wave field. Based on results of McComas and Müller (1981) and Henyey et al. (1986) for the cascade of energy in a Garrett–Munk (1975, hereafter GM) internal wave spectrum, Gregg (1989) suggested that

$$\epsilon_{IW} \propto E_{IW}^2, \tag{7}$$

where E_{IW} is the internal wave energy. Lacking direct measurements of E_{IW}, Gregg (1989) expressed internal wave-based ϵ in terms of the 10-m shear (S_{10}) and stratification (N). That is,

$$\epsilon_{G89} \propto S_{10}^4 N^2. \tag{8}$$

Other proposed formulations of the dissipation rate based on internal wave dynamics are

$$\epsilon_{GH1} \propto N^{1.0}$$

$$\epsilon_{GH2} \propto N^{1.5}$$

$$\epsilon_{GA} \propto E_{IW} N^{1.5} \tag{9}$$

(Gargett and Holloway 1984; Gargett 1990). Details of how these parameterizations are obtained are reviewed elsewhere (Gregg 1989; Wijesekera et al. 1993). Gregg (1989) stressed that his scaling arguments are based on a GM internal wave spectrum. However, his parameterization has been used to estimate mixing rates in regions where the internal waves appear to be mainly near-inertial (Marmorino and Trump 1991; D'Asaro and Morison 1992). Should any of these ϵ parameterizations work when the source of mixing is a shear layer produced by a single near-inertial wave? They do not work for a non-GM-like spectrum although modifications to the internal wave spectrum used in the parameterization improves the ϵ scaling (Wijesekera et al. 1993).

We examined the different ϵ scalings above to see if they reduce the variability in our average (YD 122–126) dissipation rate profile. The correlation between

ϵ and the vertical shear squared, S^2, is evident in the average profile for YD 122–126 (Fig. 12) below 50 m. However, ϵ is not simply related to Ri^{-1}. Above 50 m, Ri^{-1} and ϵ were both large, as expected for a mixed layer. We will not try to determine which parameterization best describes our data. Instead, we examine only the depth dependence of ϵ and determine if any of the parameterizations collapses the data to a constant value. The parameterizations of ϵ based on the internal wave energy (near-inertial energy for our data) are the poorest of the parameterizations (Fig. 13a). In fact, the depth variability has increased compared to the average ϵ profile (Fig. 12). The near-inertial energy was strongest *between* the regions of largest shear (and dissipation); hence, the poor scaling of this parameterization. The scalings based solely on the stratification reduced the ϵ variability the most (Fig. 13b), especially below the mixed layer (50 m). A higher order N-dependence would likely reduce the variability even more.

6. Summary

In this paper, we have examined the decay of a near-inertial wave over four days. From the shipboard ADCP data, we estimate that the period of this wave was 18.6 h ($\omega = 1.025f$) and the vertical wavelength (WKB-stretched using $N_0 = 3$ cph) was approximately 175 WKB-stretched-m. The clockwise rotation with depth implies that the near-inertial wave was propagating downward. We estimate that the wave was generated approximately 6 days before our arrival on station.

Over this short 4-day period, we observed the energy of the near-inertial wave to decrease by 70%. The near-inertial shear layers were regions of enhanced turbulent dissipation. We infer the source of the turbulence to be shear-induced instabilities. We estimate that 44% of the observed change in the inertial wave energy could have been lost to turbulence. Estimates of the wave energy lost at the survey site due to the wave propagating out of the region were smaller. Horizontal advection of the wave out of the survey region could have accounted for more than half of the observed energy lost; however, we did not detect the near-inertial wave during a 40 km × 40 km ADCP survey after completing the 6-day 39°N station.

The influence of this near-inertial wave on the vertical heat flux (and its divergence) in the upper thermocline will be discussed in a future paper. Also, different estimators (based on the turbulent kinetic dissipation rate and the temperature variance dissipation rate) of the vertical flux will be compared.

Acknowledgments. This work was funded by the Office of Naval Research under Grants N00014-89-J-3211 and N00014-94-10476. We thank Murray Levine, Vassilis Zervakis, and Hemantha Wijesekera for fruitful discussions on this topic. We appreciate comments made by Dan Kelley and Eric Kunze on an earlier draft of this paper. We thank the reviewers for their careful reading of the manuscript.

APPENDIX A

Complex Demodulation of the ADCP Data

Complex demodulation of a time series is used to determine the slowly varying amplitude and phase of a modulated wave of fixed frequency. We can use this technique to determine the frequency of a single wave that best describes the observed velocity or shear data. In our study, the time series consists of two velocity components, u and v, the eastward and northward velocities, respectively. We assume that the observed velocity consists of a wave with a frequency ω_0 and a slowly varying (compared to ω_0) complex amplitude and a random "noise" velocity; that is,

$$u = A(t)\exp(-i\omega_0 t) + u_n;$$
$$v = B(t)\exp(-i\omega_0 t) + v_n. \quad \text{(A1)}$$

For complex demodulation, we wish to find representative complex amplitudes A and B for a specified time period, usually several wave periods. Multiplying (A1) by $\exp(i\omega_0 t)$ and averaging over the desired period of the record (e.g., from T_1 to T_2), we have

$$\frac{1}{\Delta T}\int_{T_1}^{T_2} u\exp(i\omega_0 t)dt = \frac{1}{\Delta T}\int_{T_1}^{T_2} A(t)\exp(-i(\omega_0-\omega_0)t)dt + \frac{1}{\Delta T}\int_{T_1}^{T_2} u_n\exp(i\omega_0 t)dt$$

$$\frac{1}{\Delta T}\int_{T_1}^{T_2} v\exp(i\omega_0 t)dt = \frac{1}{\Delta T}\int_{T_1}^{T_2} B(t)\exp(-i(\omega_0-\omega_0)t)dt + \frac{1}{\Delta T}\int_{T_1}^{T_2} v_n\exp(i\omega_0 t)dt, \quad \text{(A2)}$$

where $\Delta T = T_2 - T_1$. We assume that the u_n and v_n terms average to zero over this time period. Thus,

$$\langle A\rangle = \frac{1}{\Delta T}\int_{T_1}^{T_2} u\exp(i\omega_0 t)dt;$$
$$\langle B\rangle = \frac{1}{\Delta T}\int_{T_1}^{T_2} v\exp(i\omega_0 t)dt \quad \text{(A3)}$$

and the approximated time series $\langle u\rangle$ and $\langle v\rangle$ are

$$\langle u\rangle = \langle A\rangle\exp(-i\omega_0 t); \quad \langle v\rangle = \langle B\rangle\exp(-i\omega_0 t). \quad \text{(A4)}$$

However, for our data, we do not know what value of ω_0 to use for our analysis. Therefore, we varied ω_0 and computed

$$r^2 = 1 - \frac{\int_{T_1}^{T_2} |u - \langle u \rangle|^2 + |v - \langle v \rangle|^2 dt}{\int_{T_1}^{T_2} |u|^2 + |v|^2 dt}, \quad \text{(A5)}$$

which is the fraction of explained variance. We chose ω_0 as the frequency where r^2 is a maximum. Figure A1 shows the observed u and v velocity at 122 m (solid lines in the upper panels) and the value of r^2 as a function of wave period (dotted line in the bottom panel) for a single wave complex demodulation. It is evident that there are at least two dominant waves present. One appears to be the M_2 tide; the other, a near-inertial wave. At this depth, we see that a single near-inertial wave explains more than 55% of the velocity variance, while a single wave of approximately M_2 frequency explains 30% of the variance.

After determining the complex amplitudes of u and v, $\langle A \rangle$ and $\langle B \rangle$, for the wave that best fits the velocity data, the major and minor axes of the velocity ellipse and its orientation can be determined easily. In a coordinate system oriented relative to the major and minor axes, the term $u'v'$ averaged over a wave period is zero (the primes represent quantities in the rotated coordinates). Thus, the angle of the major axis counterclockwise from east is

$$\theta = \frac{1}{2} \tan^{-1}\left[\frac{-2\,\mathrm{Re}\{\langle A \rangle \langle B \rangle^*\}}{\langle B \rangle \langle B \rangle^* - \langle A \rangle \langle A \rangle^*}\right]. \quad \text{(A6)}$$

The magnitude of the major and minor axes were obtained after rotating the complex amplitudes by this angle. [It is also possible to determine the velocity ellipse by demodulating the velocity times series as the sum of two circular oscillations in opposite directions as shown by Poulain (1990).]

It is possible to use the complex demodulation technique to determine the amplitude of two simultaneous waves (Poulain 1990). For example, if the eastward velocity is represented by

$$u = A(t) \exp(-i\omega_{M_2} t) + B(t) \exp(-i\omega_0 t) + u_n \quad \text{(A7)}$$

with $\omega_{M_2} = 2\pi / T_{M_2}$, the M_2 tide; $A(t)$, the slowly varying tidal amplitude; and $B(t)$, the slowly varying near-inertial wave amplitude. Multiplying (A7) by $\exp(i\omega_{M_2} t)$ and $\exp(i\omega_0 t)$ and averaging over a time period, we have two equations

$$\frac{1}{\Delta T}\int_{T_1}^{T_2} u \exp(i\omega_{M_2} t)dt = \langle A \rangle + \frac{1}{\Delta T}\int_{T_1}^{T_2} B \exp(-i(\omega_0 - \omega_{M_2})t)dt$$

$$\frac{1}{\Delta T}\int_{T_1}^{T_2} u \exp(i\omega_0 t)dt = \frac{1}{\Delta T}\int_{T_1}^{T_2} A \exp(-i(\omega_{M_2} - \omega_0)t)dt + \langle B \rangle. \quad \text{(A8)}$$

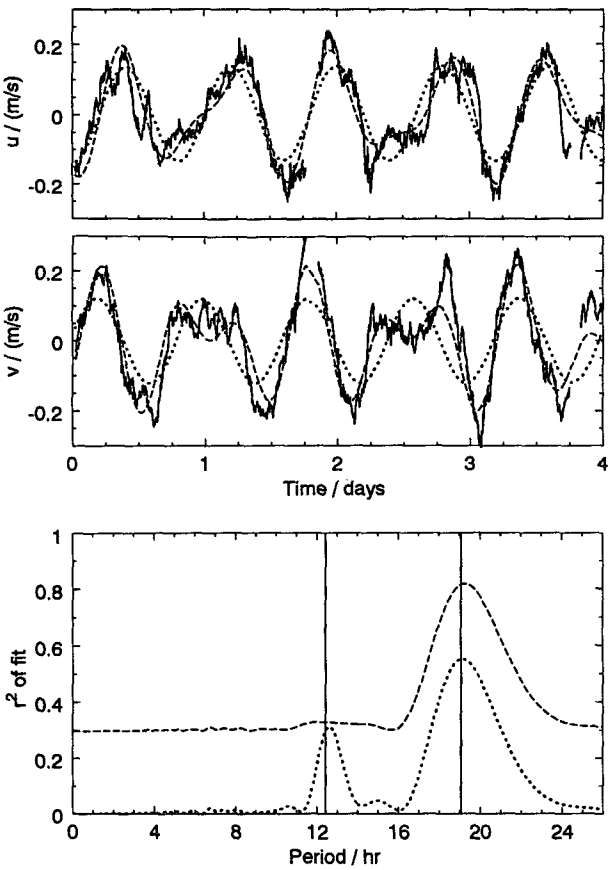

FIG. A1. Top panels: The eastward (u) and northward (v) velocity at 122 m (solid lines). Velocity time series for the single fitted wave with a period that produced the largest r^2 (dotted line) and for the M_2 tide and wave combination (dashed line) are shown. Bottom panel: The explained variance (r^2) of the complex demodulation fit of the velocity at 122 m (solid lines in the two top panels) for a single wave (dotted line) and a single wave and a 12.42-h wave (dashed line). The vertical lines show the inertial period (19.07 h) and the period of the M_2 tide (12.42 h).

Assuming that A and B are approximately constant over the averaging time, then

$$\frac{1}{\Delta T}\int_{T_1}^{T_2} A \exp(-i(\omega_{M_2} - \omega_0)t)dt = \langle A \rangle \frac{1}{\Delta T}\int_{T_1}^{T_2} \exp(-i(\omega_{M_2} - \omega_0)t)dt$$

$$\frac{1}{\Delta T}\int_{T_1}^{T_2} B \exp(-i(\omega_0 - \omega_{M_2})t)dt = \langle B \rangle \frac{1}{\Delta T}\int_{T_1}^{T_2} \exp(-i(\omega_0 - \omega_{M_2})t)dt. \quad \text{(A9)}$$

Substituting (A9) into (A8), we can solve for $\langle A \rangle$ and $\langle B \rangle$. The complex amplitudes of the two waves for the northward velocity can be determined similarly. The major and minor axes and the ellipse orientation

for both waves can be determined from the complex amplitudes as described above. As before, we can determine r^2 using

$$\langle u \rangle = \langle A \rangle \exp(-i\omega_{M_2} t) + \langle B \rangle \exp(-i\omega_0 t)$$
$$\langle v \rangle = \langle C \rangle \exp(-i\omega_{M_2} t) + \langle D \rangle \exp(-i\omega_0 t) \quad \text{(A10)}$$

in (A6). The combination of the M_2 tide and a near-inertial wave can explain more than 80% of the velocity variance between Year Days 122 and 126 (Fig. A1).

In a similar manner, the vertical shear can be complex demodulated with (dashed line in Fig. A2) and without (dotted line in Fig. A2) the M_2 tidal component. Since the M_2 tide is mainly a low vertical mode velocity field, it does not appear in the shear field. The vertical shear data has more energy in higher frequencies than the velocity data. A single near-inertial wave explains more than 60% of the observed variance in the shear data at 150 m.

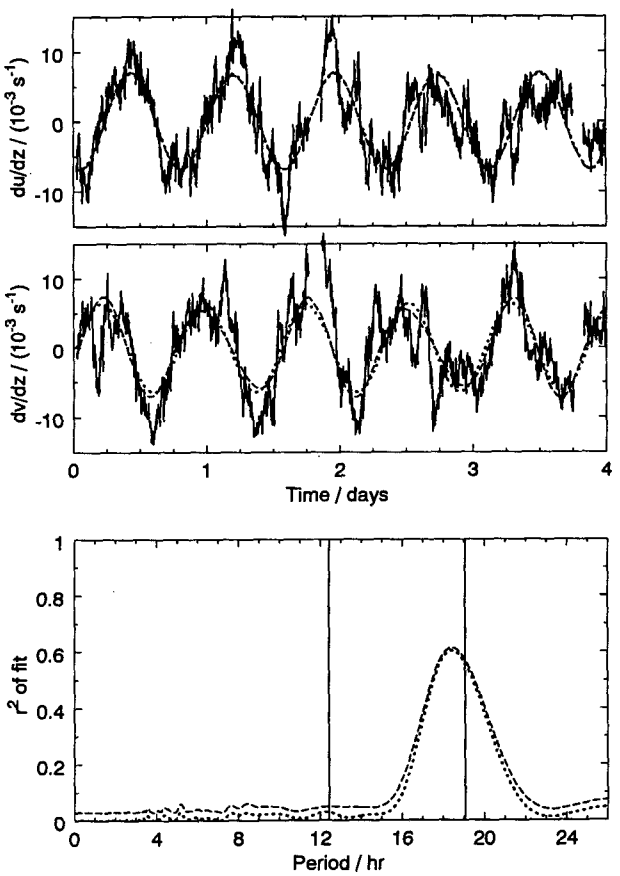

FIG. A2. Top panels: The eastward shear ($\partial u/\partial z$) and northward shear ($\partial v/\partial z$) at 150 m (solid lines). Shear time series for the single fitted wave with a period that produced the largest r^2 (dotted line) and for the M_2 tide and wave combination (dashed line) are shown. Bottom panel: The explained variance (r^2) of the complex demodulation fit of the shear at 150 m (solid lines in the two top panels) for a single wave (dotted line) and a single wave and a 12.42-h wave (dashed line). The vertical lines show the inertial period (19.07 h) and the period of the M_2 tide (12.42 h).

APPENDIX B

Complex Correlation of the ADCP Data

In our correlation analysis of the ADCP data, we define the velocity as a complex variable,

$$U = u + iv \quad \text{(B1)}$$

with u and v, the eastward and northward velocities, respectively. In determining the complex correlation for velocity $C_U(\tau)$ and shear $C_S(\tau)$, we used the unbiased estimator of the complex correlation at lag τ (Jenkins and Watts 1968). For example,

$$C_U(\tau) = \frac{1}{\sigma_U^2 (T-\tau)} \int_0^{T-\tau} U(t) U^*(t+\tau) dt, \quad \text{(B2)}$$

where σ_U^2 is the velocity variance of the time series and * represents the complex conjugate. The temporal complex correlation functions of velocity, $C_U(\tau)$, and shear, $C_S(\tau)$, oscillated near the inertial period (T_i = 19.07 h). [See Fig. 7 of Gregg et al. (1986) for an example of this oscillatory behavior.] To determine the near-inertial wave frequency and the decorrelation timescale of the wave, we examined the demodulated complex correlation of the velocity and shear data. In other words, we rotated the complex correlation back at a specified frequency to a common time (i.e., zero lag).

It is possible to estimate the frequency of the wave by examining the imaginary part of the demodulated complex correlation for different demodulation frequencies. Imagine that the velocity field consisted of a single wave with frequency ω_0,

$$U = A(t) \exp(-i\omega_0 t), \quad \text{(B3)}$$

where $A(t)$ is the constant or slowly varying complex amplitude of the wave. The complex correlation of the velocity is

$$C_U(\tau) = \frac{1}{\sigma_U^2 (T-\tau)} \int_0^{T-\tau} A(t) \exp(-i\omega_0 t) \times A^*(t+\tau) \exp[i\omega_0 (t+\tau)] dt$$
$$= \left[\frac{1}{\sigma_U^2 (T-\tau)} \int_0^{T-\tau} A(t) A^*(t+\tau) dt \right] \times \exp(i\omega_0 \tau). \quad \text{(B4)}$$

Now, if we demodulated the complex correlation $C_U(\tau)$ by our estimate of the wave frequency ω, we have

$$C_U^D(\tau) = C_U(\tau) \exp(-i\omega\tau)$$
$$= \left[\frac{1}{\sigma_U^2 (T-\tau)} \int_0^{T-\tau} A(t) A^*(t+\tau) dt \right] \times \exp[i(\omega_0 - \omega)\tau]. \quad \text{(B5)}$$

If the complex amplitude of the wave does not oscillate rapidly compared to ω_0, the $[\cdot]$ term in (B5) has no imaginary component. Thus, if $\omega = \omega_0$, then the imaginary component of C_U^D would be zero for all lags. Otherwise, the complex correlation would oscillate with a frequency that is the difference between the wave frequency and the demodulated frequency. If the true wave frequency ω_0 was slightly higher than the estimated frequency ω, the imaginary component of the demodulated complex correlation function would increase with increasing lag. Similarly, if the true frequency was slightly less than ω, the imaginary component of the demodulated correlation would decrease with increasing lag.

REFERENCES

Caldwell, D. R., T. M. Dillon, and J. N. Moum, 1985: The rapid sampling vertical profiler—an evaluation. *J. Atmos. Oceanic Technol.*, **2,** 615–625.

Chereskin, T. K., J. N. Moum, P. J. Stabeno, D. R. Caldwell, and C. A. Paulson, 1986: Fine-scale variability at 140°W in the equatorial Pacific. *J. Geophys. Res.*, **91,** 12 887–12 897.

D'Asaro, E. A., 1985: The energy flux from the wind to near-inertial motions in the surface mixed layer. *J. Phys. Oceanogr.*, **15,** 1043–1059.

——, 1989: The decay of wind-forced mixed layer inertial oscillations due to the β effect. *J. Geophys. Res.*, **94,** 2045–2056.

——, and J. H. Morison, 1992: Internal waves and mixing in the Arctic Ocean. *Deep-Sea Res.*, **39,** S459–S484.

Efron, B., and G. Gong, 1983: A leisurely look at the bootstrap, the jackknife, and cross-validation. *Amer. Stat.*, **37,** 36–48.

Gargett, A. E., 1990: Do we really know how to scale the turbulent kinetic energy dissipation rate ϵ due to breaking of oceanic internal waves? *J. Geophys. Res.*, **95,** 15 971–15 974.

——, and G. Holloway, 1984: Dissipation and diffusion by internal wave breaking. *J. Mar. Res.*, **42,** 15–27.

Garrett, C. J. R., and W. H. Munk, 1975: Space-time scales of internal waves: A progress report. *J. Geophys. Res.*, **80,** 291–297.

Gill, A., 1984: On the behavior of internal waves in the wakes of storms. *J. Phys. Oceanogr.*, **14,** 1129–1151.

Gregg, M. C., 1989: Scaling turbulent dissipation in the thermocline. *J. Geophys. Res.*, **94,** 9686–9698.

——, and T. B. Sanford, 1988: The dependence of turbulent dissipation on stratification in a diffusively stable thermocline. *J. Geophys. Res.*, **93,** 12 381–12 392.

——, E. A. D'Asaro, T. J. Shay, and N. Larson, 1986: Observations of persistent mixing and near-inertial internal waves. *J. Phys. Oceanogr.*, **16,** 856–885.

Hebert, D., J. N. Moum, C. A. Paulson, and D. R. Caldwell, 1992: Turbulence from internal waves at the equator. Part II: Details of a single event. *J. Phys. Oceanogr.*, **22,** 1346–1356.

Henyey, F. S., J. Wright, and S. M. Flatté, 1986: Energy and action flow through the internal wave field: An eikonal approach. *J. Geophys. Res.*, **91,** 8487–8495.

Jenkins, G. M., and D. G. Watts, 1968: *Spectral Analysis and its Applications.* Holden-Day, 525 pp.

Kunze, E., M. G. Briscoe, and A. J. Williams III, 1990: Interpreting shear and strain fine structure from a neutrally buoyant float. *J. Geophys. Res.*, **95,** 18 111–18 125.

——, R. W. Schmitt, and J. M. Toole, 1994: The energy balance in a warm core ring's near-inertial critical layer. *J. Phys. Oceanogr.*, submitted.

Lien, R.-C., M. J. McPhaden, and D. Hebert, 1994: Intercomparison of ADCP measurements at 0°, 140°W. *J. Atmos. Oceanic Technol.*, **11,** 1334–1349.

Marmorino, G. O., and C. L. Trump, 1991: "Turbulent Mixing" induced by upgoing near-inertial waves in the seasonal thermocline of the Norwegian Sea. *J. Geophys. Res.*, **96,** 7137–7143.

——, L. J. Rosenblum, and C. L. Trump, 1987: Fine-scale temperature variability: The influence of near-inertial waves. *J. Geophys. Res.*, **92,** 13 049–13 062.

McComas, C. H., and P. Müller, 1981: The dynamical balance of internal waves. *J. Phys. Oceanogr.*, **11,** 970–986.

Moum, J. N., D. R. Caldwell, and C. A. Paulson, 1989: Mixing in the equatorial surface layer and thermocline. *J. Geophys. Res.*, **94,** 2005–2021.

——, D. Hebert, C. A. Paulson, and D. R. Caldwell, 1992: Turbulence and internal waves at the equator. Part I: Statistics from towed thermistors and a microstructure profiler. *J. Phys. Oceanogr.*, **22,** 1330–1345.

Munk, W., 1981: Internal waves and small scale processes. *Evolution of Physical Oceanography: Scientific Surveys in Honor of Henry Stommel,* B. A. Warren and C. Wunsch, Eds., The MIT Press, 264–291.

Oakey, N. S., 1982: Determination of the rate of dissipation of turbulent energy from simultaneous temperature and velocity shear microstructure measurements. *J. Phys. Oceanogr.*, **12,** 256–271.

Pollard, R. T., 1969: On the generation by winds of inertial waves in the ocean. *Deep-Sea Res.*, **17,** 795–812.

Poulain, P.-M., 1990: Near-inertial and diurnal motions in the trajectories of mixed layer drifter. *J. Mar. Res.*, **48,** 793–823.

Rubenstein, D. M., 1983: Vertical dispersion of inertial waves in the upper ocean. *J. Geophys. Res.*, **88,** 4368–4380.

Sanford, T. B., 1991: Spatial structure of thermocline and abyssal internal waves. *Dynamics of Oceanic Internal Gravity Waves, Proc. 'Aha Huliko'a, Hawaiian Winter Workshop,* P. Müller and D. Henderson, Eds.

Toole, J. M., and R. W. Schmitt, 1987: Small-scale structures in the north-west Atlantic sub-tropical front. *Nature,* **327,** 47–49.

Wijesekera, H., L. Padman, T. Dillon, M. Levine, C. Paulson, and R. Pinkel, 1993: The application of internal-wave dissipation models to regions of strong mixing. *J. Phys. Oceanogr.*, **23,** 269–286.